

Ring mechanism of fast Na⁺ ion transport in Na₂LiFeTeO₆: Insight from molecular dynamics simulation

Kartik Sau ^{1,2,3,*} and Tamio Ikeshoji²

¹Research Institute of Electrochemical Energy (RIECEN), National Institute of Advanced Industrial Science and Technology (AIST),
1-8-31 Midorigaoka, Ikeda, Osaka 563-8577, Japan

²Mathematics for Advanced Materials Open Innovation Laboratory (MathAM-OIL), National Institute of Advanced Industrial Science
and Technology (AIST), c/o Advanced Institute for Materials Research (AIMR), Tohoku University, Sendai 980-8577, Japan

³Advanced Institute for Materials Research (AIMR), Tohoku University, Sendai 980-8577, Japan



(Received 21 November 2021; accepted 12 April 2022; published 29 April 2022)

Honeycomb-layered oxides have attracted recent attention because of their rich crystal chemistry. However, the atomistic mechanisms of cationic transport in these structures remain vastly unexplored. Herein, we perform an extensive, systematic molecular dynamics study on Na₂LiFeTeO₆ using combined force-field and first-principles-based molecular dynamics simulations. We use a refined set of interatomic potential parameters of a previously reported potential model that represents various structural and transport properties of this recently reported promising material for all-solid-state battery applications. The present simulation study elucidates the roles of octahedral ordering and entropic contributions in Na⁺ ion distribution in the *ab* plane. Our theoretical simulation also develops a ringlike atomistic diffusion mechanism and relevant atomistic energy barriers that help to understand the origin of fast ion conduction in honeycomb-layered oxides.

DOI: [10.1103/PhysRevMaterials.6.045406](https://doi.org/10.1103/PhysRevMaterials.6.045406)

I. INTRODUCTION

The improvement of high-energy-density batteries is a major focus in current research [1] owing to consumer demand for sophisticated electronic gadgets and the ever-increasing demand for electric vehicles. Conventional Li-ion batteries cannot satisfy present demand, whereas all-solid-state batteries (ASSB) could be suitable because of favorable factors such as high volumetric and gravimetric energy density, safety, and long life cycle. Fast ion conducting (FIC) solids form an integral part of ASSB and are a leading topic of current research [2–4]. Significant efforts have been devoted over the last three decades to the advancement of Li⁺ ion conducting materials [5–14]. Recently, sodium ion conductors have been reported to be promising for energy storage applications because the Na ion has a very similar intercalation chemistry to the Li ion and, in some cases, the Na ionic radius is more suitable for stabilizing fast ion conducting frameworks because of its larger size compared with the Li ionic radius. Thus, the development of sodium ion conducting ASSB working at ambient temperatures is gaining renewed attention. Recently, a unique class of heterostructures known as honeycomb-layered oxides has gained attention as high-energy-density electrodes and electrolyte materials for their rich crystal chemistry that provides high cationic conduction [15–27]. The structure in general consists of an array of parallel transition metal slabs with a distinct honeycomb arrangement sandwiching of alkali-metal atoms.

Atomistic details are valuable for better understanding and development of FIC solids [28]. Molecular dynamics (MD) simulation has emerged as one of the first simulation methods for its ability to elucidate the underlying mechanisms at atomic level [29], as a complement to experimental probes, which are often difficult to implement. Recently, we developed an interatomic potential model for a family of FICs A₂M₂TeO₆ (A = Li, Na, or K; M = Ni, Zn, Co, or Mg) [30,31] to perform MD studies that represent the structural and dynamical properties reported in the experiments and present several interesting behaviors such as energy-driven or entropy-driven diffusion depending on the concentration of the mobile ions. Moreover, the simulated cationic path in Na₂Ni₂TeO₆ has been experimentally confirmed [32,33]. Accurately depicting microscopic physicochemical properties of materials that are beyond experimental reach requires the use of reliable potential parameters that can effectively reproduce the structural and transport properties determined by experiment. In this context, first-principles MD (FPMD) simulation, which reproduces forces on atoms precisely from electronic structure, will play a major role. However, FPMD is computationally extremely expensive and cannot deal with larger system sizes and longer time behaviors. Therefore, achieving accurate diffusion behavior is difficult because of low statistical accuracy. Thus, we rely on force-field-based MD simulations.

The present MD simulations are motivated by the recent experimental studies by Nalbandyan *et al.* [34], who synthesized a fast Na⁺-conducting solid (0.04 S/cm at 573 K comparable with the β-alumina [35–38]) of the formula Na₂LiFeTeO₆. The material is isostructural with

*kartik.sau@gmail.com

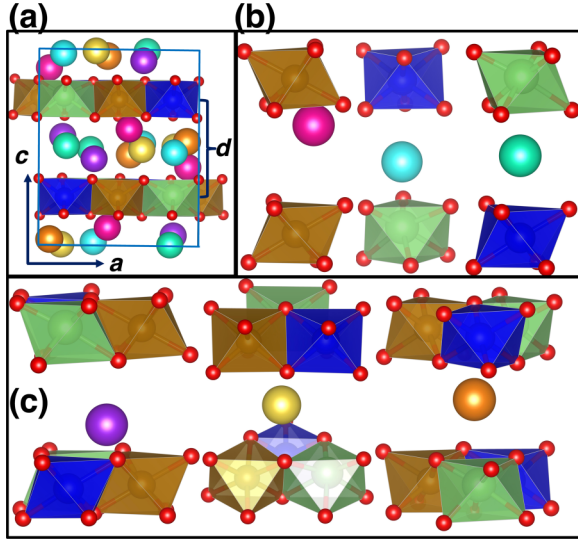


FIG. 1. A schematic of the $\text{Na}_2\text{LiFeTeO}_6$ orthorhombic crystal structural framework whereby parallel slabs comprising LiO_6 octahedra (in green), FeO_6 octahedra (in brown), and TeO_6 octahedra (in ash) are separated by Na atoms denoted with various colors. (a) Li (in light green), Fe (in brown), and Te (in blue) in octahedral coordination with oxygen atoms (in red). Blue lines denote the unit cell and the interlayer distance is marked by d . (b) Several crystallographically distinct sites with face-sharing framework octahedra in which Na ions reside, denoted as Na1 (in orange), Na2 (in yellow), and Na3 (in purple). (c) Na sites Na4 (in magenta), Na5 (in green), and Na6 (in cyan), with edge-sharing framework octahedra. The local polyhedral environments are also shown, for clarity. The a and c axes are also shown. The occupancies at the different Na sites are 0.022, 0.958, 0.074, 0.038, 0.901, 0.019 for Na1, Na2, Na3, Na4, Na5, and Na6, respectively. Essentially, the other Na-site occupancies are negligible apart from the Na2 and Na5 sites at room temperature.

heterovalence analogs of $A_2M_2\text{TeO}_6$ ($A = \text{Na, K}$; $M = \text{Ni, Zn, Co, and Mg}$), consisting of edge-sharing LiO_6 , FeO_6 , and TeO_6 octahedral brucitelike layers spanning the ab plane, in which Te alternates with Li or Fe. It is worth noting that the other materials in this series are mainly used as electrode, whereas these materials are used as an electrolyte with indium electrodes [34]. The brucitelike octahedral layers are not identical along the c axis, unlike the structure $A_2\text{Ni}_2\text{TeO}_6$ ($A = \text{Na, K}$), where the Na^+ ions occupy the interlayer, as furnished in Fig. 1. Despite the immense potential envisioned in the experimental study, detailed theoretical explorations of honeycomb-layered materials, such as surrounding of the various mesoscopic mechanisms engendering their remarkable electrochemical performance, still remain unexplored. Specifically, local octahedral interlayer influencing on ionic conductivity is unclear, as the interlayer distance is determined by existing elements in the framework octahedral layer and by mobile ions within the framework interlayer, and cationic diffusion mechanism such as ring mechanism, which also plays a significant role in diffusion elsewhere [39,40]. This study on this material provides full interatomic potentials and fresh insights on ion transport. We developed the potential parameters for carrying out force-field-based MD study and

TABLE I. Interionic potential parameters employed in this study. $A_{\text{Na-Na}} = 0$ eV, $A_{\text{Na-Li}} = 80\,000$ eV, $A_{\text{Na-Fe}} = 27\,000$ eV, $A_{\text{Na-Te}} = 7\,000$ eV, $n_{\text{Na-Na}} = n_{\text{Na-Li}} = n_{\text{Na-Fe}} = n_{\text{Na-Te}} = 11$.

Species (M)	q_M (C)	$\tilde{\sigma}_M$ (Å)	A_{M-O} (eV)	C_{M-O} (eV Å ⁶)	P_{M-O} (eV Å ⁴)	n_{M-O}
Na	0.65 ^a	1.13 ^a	0.1202	0.0 ^a	0.0 ^a	9
Li	0.65	0.76	1.220	0	12	9
Fe	1.95	0.86	1.011	35.85	19	9
Te ^a	3.90	0.70	3.9098	17.15	11.3	9
O ^a	-1.30	1.21	0.106	85.14	0.0	7

^aThe value used from the reported literature [30,41].

confirmed their reliability by a first-principles calculation of structural properties.

II. METHODOLOGY

A. Interatomic potential

To carry out an MD simulation, the reported Vashishta-Rahman form of interatomic potential [42] is employed. This method is becoming popular recently, as it describes structural and dynamical properties of a series of honeycomb-layered oxides, namely $\text{Na}_2M_2\text{TeO}_6$ ($M = \text{Ni, Zn, Co, and Mg}$) [30], as well as Na-superionic conductors (NASICONs). This potential form is softer in nature than the other widely used Born-Mayer (Buckingham) [43] and Lennard-Jones potentials [44]. The Vashishta-Rahman potential form is as follows [42]:

$$V_{ij}(r_{ij}) = \frac{q_i q_j}{r_{ij}} + \frac{A_{ij}(\tilde{\sigma}_i + \tilde{\sigma}_j)^{n_{ij}}}{r_{ij}^{n_{ij}}} - \frac{P_{ij}}{r_{ij}^4} - \frac{C_{ij}}{r_{ij}^6}, \quad (1)$$

where q_i represents the charge and $\tilde{\sigma}_i$ the ionic radius of the i th atom. The parameters A_{ij} , P_{ij} , and C_{ij} describe the overlap-repulsion energy of the electron clouds, the average charge dipole interactions, and the dispersion constant between the ion pairs i and j , respectively. The Vashishta-Rahman potential has a softer overlap repulsion ($1/r^n$, where $n = 11, 9$, or 7 for cation-cation, cation-anion, and anion-anion pairs, respectively), particularly between the anion-anion pairs. The interatomic parameters used in this study are listed in Table I. Some of the parameters have already been reported [30]. The parameters that are unavailable in the literature were determined using empirical fitting to attain the experimentally reported bond lengths (Li-O, Fe-O, and O-O) of $\text{Na}_2\text{LiFeTeO}_6$ [30,45–47]. The details of the empirical fitting methods are as follows: The nonidentical brucitelike octahedral framework along the c axis is retained by refining the Li-Na, Fe-Na, and Te-Na pairs and the Na-O parameters were refined to represent the conductivity. We use high value of $A_{\text{Na-Li}}$ to compensate a lower Na-Li Coulomb repulsion, whereas a lower value of $A_{\text{Na-Te}}$ is used because of the higher Coulomb repulsion.

B. Computational details

The empirically fitted set of parameters listed in Table I were used to carry out a series of MD simulations in the temperature range of 400 to 700 K with 25-K intervals, and zero atmospheric pressure. The Parrinello-Rahman isobaric-isothermal (NPT) MD method [48], which allows for changes

in the simulation box sizes while keeping angles fixed, was used. The temperatures and pressure in the system were controlled using thermostating and barostating techniques, whereby some dynamic variables are coupled with particle velocities and simulation box dimensions. Simulations commenced from the reported x-ray diffraction structures [34] wherein the simulation supercell was constructed by $7 \times 4 \times 3$ unit cells comprising 3696 atoms in an orthorhombic symmetry following $P2_12_12_1$ (No. 19). Several partially occupied crystallographic sites were identified in the Na conduction plane. In MD simulations, we placed the Na⁺ ions at the crystallographically reported highly occupied sites (Na2 and Na5) to avoid strong cation-cation repulsion, as number of Na2 and Na5 sites are the same (two for each layer per unit cell and the total is four in each layer) as number of available Na ions (four in each layer). Thus, others crystallographic Na sites are vacant. Even though there are several vacant Na sites, the material is stoichiometric. The initial Na⁺ ion configuration can be done by several possible ways, using criteria that the Na⁺ ions can not be placed at a very short distance. For clarity, all reported crystallographically distinct sites (Na1, Na2, Na3, Na4, Na5, and Na6) along with the site occupancy [34] in the layered frameworks of Na₂LiFeTeO₆ are shown in Fig. 1. The interlayer interaction is usually weaker in nature; thus, interlayer sliding is expected unless the initial configuration is not set properly. To avoid interlayer sliding, we performed a constrained MD simulation for 500 ps for each temperature case; the framework atoms (Li, Fe, and Te) were frozen at the crystallographic sites and the other atoms were allowed to move. Finally, we lifted the former constraint and performed the usual MD simulation. A time step of 2 fs was applied to the velocity Verlet algorithm to solve Newton equations of motion and the dynamical variables for controlling temperature and pressure (Nose-Hoover thermostat and barostat) are 100 and 1000 times of time step, respectively, using the LAMMPS software package [49]. The above-mentioned values are default in LAMMPS. A typical runtime of 6 ns or longer was used with trajectory samples stored at intervals of 200 fs for detailed analyses. To guarantee the thermodynamic convergence properties, a few longer runtime simulations of 100 ns were performed separately. The properties remained the same for longer time simulation. Periodic boundary conditions in all three directions and the Ewald summation technique for the convergence of long-range Coulombic interactions were applied. A cutoff distance of 13 Å was used for both the short-range interactions and the short-range part of the Ewald summation. Microcanonical MD (NVE-MD) simulations were further performed at 600 K using the final structure obtained from NPT-MD simulations for cationic density calculation.

Furthermore, to understand the entropy effect in the presence of a larger number of Na⁺ ions, we performed a few MD simulations with a different number of Na⁺ ions in each layer maintaining the material stoichiometry. For instance, there are four Na⁺ ions in each layer in each unit cell. Here, we performed two distinct NPT-MD simulations with alternative Na⁺ ion densities as follows:

(1) The first layer contains three Na⁺ ions (normally four), whereas five Na⁺ ions were placed at Na sites in the next layer. We call this scenario underloaded case 1.

(2) The first layer contains two Na⁺ ions (normally four), whereas six Na⁺ ions were placed at Na sites in the next layer. We call this scenario underloaded case 2.

We constructed two such supercells additionally, which also maintain charge conservation, and performed NVE-MD simulations followed by NPT-MD simulations at 600 K.

Finally, first-principles optimization and FPMD simulation were performed based on density functional theory (DFT) using the Vienna *ab initio* simulation package (VASP) [50,51] to compare the structure with that obtained using the force-field-based MD simulation. The structural optimization was performed by placing the Na⁺ ions at Na sites using several combinations or configurations for understanding the Na⁺ ion favorable occupancy at the different Na sites. The energies of all such configurations (placing Na⁺ ion at Na2 and Na3, or at Na5 and Na6, or at Na2 and Na5) were compared and the detailed energies shall be discussed in Sec. III. We performed FPMD simulations in an NPT ensemble, in which temperature and pressure were controlled using Langevin thermostating and barostating techniques. The plane-wave basis sets and projector-augmented-wave pseudopotentials [52,53] were used under periodic boundary conditions. An energy cutoff of 700 eV was used; integrals over the Brillouin zone were performed only at the Γ point. A Perdew-Burke-Ernzerhof (PBE) functional was used for the exchange correlation with a generalized gradient approximation (GGA). Spin-polarized GGA+*U* approach was applied for Na₂LiFeTeO₆. The simulated supercell consisted of $2 \times 1 \times 1$ unit cells with a total of 88 atoms. The FPMD simulations were performed at 300 and 800 K for 1-ps equilibration and 2-ps sampling with a time step of 1 fs. The intention of high-temperature FPMD simulation was because of the Na⁺ ion diffusion. However, it is difficult to obtain Na⁺ ion diffusion within such short simulated time periods and smaller number of atoms (88).

C. Estimation of key quantities

The ion transport is calculated from the mean-square displacement (MSD) of Na⁺ following Einstein's relation. The self-diffusion coefficient is calculated from the slope of the MSD for the two-dimensional transport as

$$\text{MSD} = \frac{1}{N} \left\langle \sum_{j=1}^N [\vec{r}_j(t+t') - \vec{r}_j(t)]^2 \right\rangle, \quad (2a)$$

$$D = \lim_{t \rightarrow \infty} \frac{\text{MSD}}{4t'}, \quad (2b)$$

where N denotes the total number of mobile atoms in the system, $\vec{r}_j(t)$ is the position vector of the j th ion at time t , t' is the time difference, and the angular brackets indicate the average over several points in time. The factor 4 appearing in the denominator of Eq. (2b) is because of two-dimensional diffusion, whereas it is six for the three-dimensional case. The diffusion coefficient D depends on the temperature (T) according to the Arrhenius equation

$$D = D_0 \exp\left(\frac{-E_a}{k_B T}\right), \quad (3)$$

where D_0 is the preexponential factor, E_a represents the activation energy of ion hopping, and k_B is the Boltzmann constant.

The conductivity σ can be linked to the diffusion coefficient D according to the Nernst-Einstein equation

$$\sigma = \frac{nq^2D}{H_r k_B T}, \quad (4)$$

where n is the carrier density, q represents the formal charge of the mobile cation, and H_r is Haven ratio, which is assumed to be one for the present system. By substituting these relationships into Eq. (3), one can write

$$\sigma T = \frac{nq^2 D_0}{k_B} \exp\left(\frac{-E_a}{k_B T}\right), \quad (5a)$$

$$\ln(\sigma T) = \ln\left(\frac{nq^2 D_0}{k_B}\right) - \frac{E_a}{k_B T}. \quad (5b)$$

The potential energy of the individual cations is calculated as

$$V_i = \frac{1}{2} \sum_{j=1}^N V_{ij}, \quad (6)$$

where V_{ij} is the interaction potential given in Eq. (1), such that the total potential energy of the system is

$$V_t = \sum_{i=1}^N V_i. \quad (7)$$

The relative free energy as seen by the individual cations ΔF can be measured relative to another system of cations at the location on the ab plane exhibiting the maximum cation population density p_{\max} according to the formula [46,54–56]

$$\Delta F = -k_B T \ln\left(\frac{p}{p_{\max}}\right) = \Delta V - T \Delta S, \quad (8)$$

where p represents the population density function (the occupancy) of the cations, p_{\max} is the maximum value of the population density function, ΔV is the difference in potential energy of the individual cations [Eq. (4)], and ΔS is the difference in entropy (the relative entropy).

Finally, we calculated the self part of the van Hove correlation function $G_S(r, t')$ to understand the Na^+ ion hopping mechanism using the formula [57]

$$G_S(r, t') = \frac{1}{N} \left\langle \sum_{i=1}^N \delta(\vec{r} - (\vec{r}_i(t' + t) - \vec{r}_i(t))) \right\rangle. \quad (9)$$

III. RESULTS AND DISCUSSION

A. Framework polyhedral structure

The $\text{Na}_2\text{LiFeTeO}_6$ structure consists of several polyhedral interlayers with sandwiching Na^+ ions, as shown in Fig. 1 reported by Nalbandyan *et al.* [34]. The top and the bottom of the adjacent framework interlayers are not identical, unlike the other materials $A_2\text{Ni}_2\text{TeO}_6$ ($A = \text{Na}$, and K). The LiO_6 , FeO_6 , and TeO_6 octahedra are arranged in a honeycomb fashion inside the framework layer. The octahedral interlayers are stabilized along the c axis by Van der Waals forces and by interactions mediated via the Na atoms occupying the interlayers. To understand octahedral ordering, an octahedral density pattern of $\text{Na}_2\text{LiFeTeO}_6$ along the y direction from

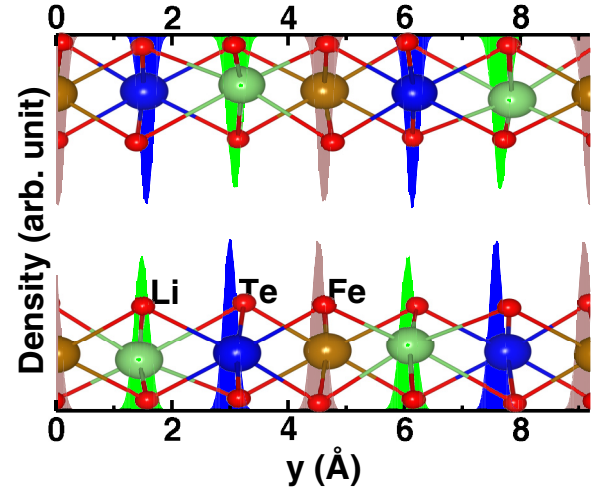


FIG. 2. Atomic distribution of octahedral center atoms along the y axis. The octahedral center atoms Li , Te , and Fe are marked in light green, blue, and brown, respectively, at 300 K for $\text{Na}_2\text{LiFeTeO}_6$ from NPT-MD force-field-based simulations. The corresponding crystallographic octahedral layers [34] are also shown in ball-and-stick model using the same color coding for comparison.

MD simulation is shown in Fig. 2, in which the FeO_6 octahedra are located on the top and the bottom along the c axis. The Na^+ ion density pattern in the conduction plane is significantly influenced by the local octahedral sequences, most importantly where the interlayer distance is small (~ 3.5 Å). The octahedral density pattern from MD simulation follows the same ordering as reported in x-ray structure. The interlayer octahedral density is found to be slightly off particularly at high temperatures because of thermal oscillation that leads to polyhedral layer sliding. Furthermore, the average cell parameters of $\text{Na}_2\text{LiFeTeO}_6$ calculated from NPT-MD simulations at 300 K are comparable to the experimental reported cell parameters, with about 1.5% deviation, as shown in Table II, validating the potential model. To obtain a more detailed structural comparison, we also calculated radial distribution functions $g(r)$ between the framework atom pairs Li-O , Fe-O , Te-O , and O-O , obtained from NPT-MD simulations at 800 K and from FPMD at 800 K for $\text{Na}_2\text{LiFeTeO}_6$ (Fig. 3). All calculated peaks from MD simulations are consistent with their corresponding $g(r)$, calculated for the x-ray diffraction (XRD) structure and FPMD, although thermal broadening is observed. Whereas, a sharper peak from force-field-based MD simulations indicates stiffer interatomic potential param-

TABLE II. A comparison of average cell parameters (in Å) calculated from isobaric-isothermal (NPT) MD simulations performed at 300 K for the $\text{Na}_2\text{LiFeTeO}_6$ from both FPMD and force-field based with reported experimental results (abbreviated as “Expt.”). $\delta = \left| \frac{\text{Expt.}-\text{MD}}{\text{Expt.}} \right| \%$.

Cell parameters	Expt. [34]	MD	FPMD	δ
a	5.21	5.29	5.21	1.5
b	8.99	9.11	8.98	1.5
c	11.24	11.41	11.25	1.5

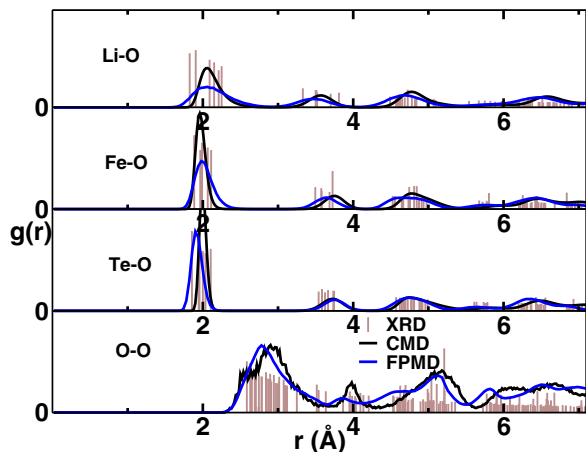


FIG. 3. Radial distribution function [$g(r)$] between selected ion pairs (namely, Li-O, Fe-O, Te-O, and O-O) at 800 K for $\text{Na}_2\text{LiFeTeO}_6$ from NPT-MD simulations based on both force-field MD and FPMD (at 800 K). For clarity, the vertical bars shown in brown are the corresponding radial distribution functions derived from x-ray diffraction analyses [34]. The bar heights are reduced for easy visualization.

eters. It could be possibly because of the structural disordered (different B -O bond distance; $B = \text{Li, Fe, and Te}$), whereas we employed a single type of pair of interaction for simplicity of the potential model. The Li, Fe, and Te atoms have exactly six O atoms within their respective bond distances, as shown in Fig. S1 in the Supplemental Material [58]. The bond lengths are also close to the experimental reported bond distances, affirming that the present set of interatomic parameters reasonably represents the local structure as well as the octahedral sequences.

B. Ionic conductivity

For further confirmation of structural stability, we calculated the mean-square displacement (MSD) of the framework atoms (Li, Fe, Te, and O), as displayed in Fig. 4(b). The MSDs

of the framework atoms are almost negligible, indicating rigidity of the framework structure. Herein, we want to emphasize that the Li atoms form immobile framework because of the crystallographic location of the Li atoms coordinated. We calculated the energy of the Li atoms at their crystallographic location, where potential energy minima (-5.81 eV) are significantly deeper than the average potential energy of Na^+ ions (-0.27 eV). The deeper potential energy minima at the Li sites is because of the six octahedral coordinated oxygen atoms at a closer distance (~ 2 Å), whereas the Na ions are located at a far distance (~ 3.5 Å) and the coordination numbers are also low (less than 2), shown in Fig. S2 in the Supplemental Material [58]. In contrast, the loose coordination to the framework polyhedral interlayer allocates several Na sublattices in the conduction layer for facile cationic conduction, as identified in the reported experimental structure. The facile Na^+ ion diffusion is reflected in the plot of the mean-square displacements (MSD) against time [Fig. 4(a)]. The closely packed framework octahedral layers parallel to the ab plane restrict the Na^+ ion diffusion along the c -axis direction of the cell, as reflected in the inset of Fig. 4(b) (less than 0.04 Å² [59]). Therefore, cationic mobility appears to be restricted within the sublattices oriented parallel to the ab plane, affirming the diffusion to be highly anisotropic (or layer diffusion), as also observed in the previous studies [20,60].

The Na^+ ion conductivity σ is calculated from the diffusion coefficient D (the slope of the MSD in the diffusive region), according to Eq. (4). Calculation of the conductivity is also possible using the Green-Kubo relation instead of the Nernst-Einstein equation (3). In principle, both approaches are equivalent. However, the correlation function involved in the Green-Kubo formula shows a slow decay or what is referred to as long-time tail [61] that includes large fluctuations in the calculated electrical conductivity at long times [62–64]. The plot of the logarithm of σT versus the inverse temperature ($1000/T$) is displayed in Fig. 5. The simulated result displays a straight line indicating Arrhenius behavior, whereas the experimental result shows a deviation from linearity at high temperature, possibly because of a phase transition. The activation energy can be calculated from the slope of the

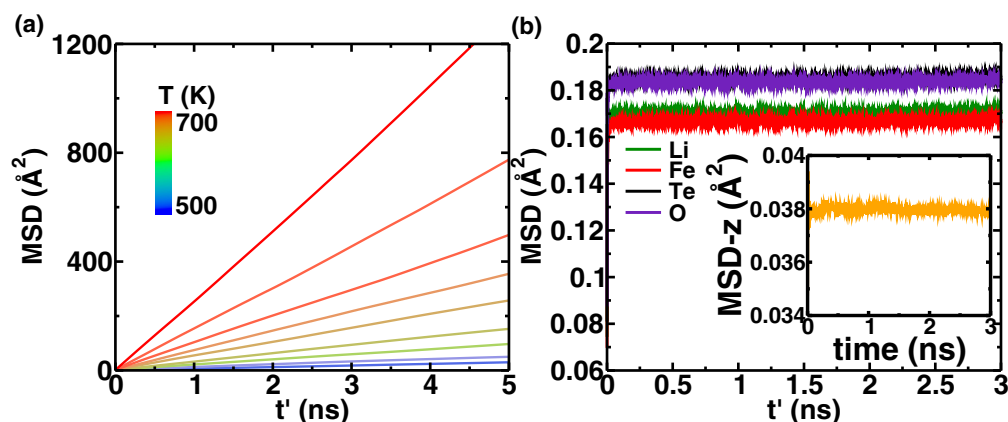


FIG. 4. (a) Mean-square displacement (MSD) of Na^+ ions against time difference t' in $\text{Na}_2\text{LiFeTeO}_6$ based on canonical (NVT) MD simulations for the temperature range of 500–700 K at 25-K intervals. (b) MSD of the framework atoms at 600 K. Inset shows the MSD of Na^+ ions along the c -axis direction (MSD- z) at 600 K. These results demonstrate that the framework atoms are immobile and the Na^+ ions are restricted along the ab plane, rendering the diffusion to be highly anisotropic.

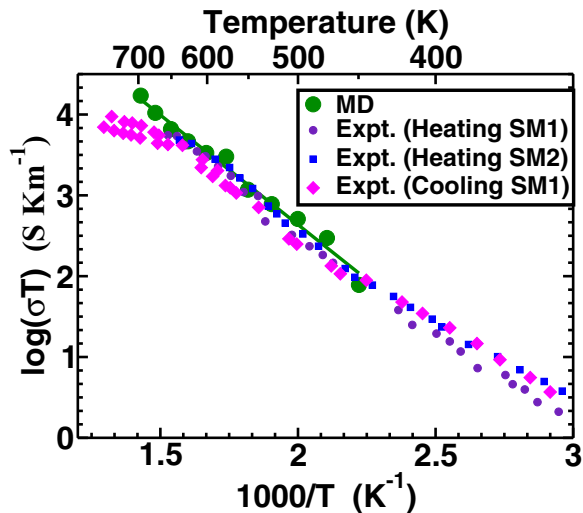


FIG. 5. Arrhenius plots of the Na^+ ions in $\text{Na}_2\text{LiFeTeO}_6$ from molecular dynamics (MD) simulation results for the temperature range of 450 to 700 K at intervals of 25 K. A fitted line (green) is also shown. For the comparison, the experimentally obtained Arrhenius plots for heating and cooling (where SM1 and SM2 indicate experimental samples from two different synthesis methods [34]) are reproduced, along with the MD simulation results. The activation energies calculated from both experimental (0.48 eV) and MD simulation results ($0.54 \pm 0.02 \text{ eV}$) are close. The error in the activation energy is the standard error of the least-square fit.

straight line according to Eq. (3). The activation energy of $\text{Na}_2\text{LiFeTeO}_6$ is found to be $0.54 \pm 0.02 \text{ eV}$ from the MD simulation, whereas 0.48 eV is reported from the experimental study [34]. Therefore, we conclude that the present MD simulation model successfully represents the structural (framework octahedral orientation and radial distribution functions) and dynamical properties of $\text{Na}_2\text{LiFeTeO}_6$ with reasonable experimental agreement.

C. Atomistic mechanisms of Na^+ ion transport

Herein, our focus is on the atomistic origin of high ionic conductivity in $\text{Na}_2\text{LiFeTeO}_6$. We calculated the three-dimensional isosurface population density along with the polyhedral framework, as shown in Figs. 6(a) and 6(b) for understanding of Na^+ ion transport path. The Na^+ ion density lies inside the octahedral framework layer, which is also reflected in the MSD plot of the Na^+ ions along the z direction. For further clarity of the Na^+ ion diffusion paths, the two-dimensional population density (the number of ions per unit area) pattern and the average potential energy of the Na^+ ions in the conduction layer are also presented in Figs. 6(c) and 6(d). The average potential energy of the individual cations is calculated using Eq. (6) (detailed in Sec. II) and projected onto a two-dimensional (2D) grid in the ab plane. Both the projected population density and the average potential energy are also replicated in 2×2 unit cells in the conduction plane for continuity, as shown in Figs. 6(c) and 6(d). The high-density areas and their local environment octahedral centers and the Na sites are indicated on top of the density and energy patterns.

TABLE III. A comparison of the total-energy difference for several Na^+ ion initial configurations at different Na sites calculated from DFT-based optimized structures (the lowest-energy value is chosen as zero, while the Na^+ ions were placed at Na2 and Na5 sites).

Combination of Na sites	Total-energy difference/ formula unit (eV)
Na2-Na3	4.4
Na5-Na6	0.3
Na2-Na5	0.0

There are five high-density maxima in the population density profile, whereas there are four available Na^+ ions per unit cell per interlayer. Therefore, the Na^+ ions can occupy the high-density maxima and can diffuse as well through the available vacant sites; as a result, the occupancy at each high-density area has to be less than unity. Such available vacant site plays a significant role on high cationic diffusion that will be discussed later in the Na^+ ion diffusion mechanism. The occupancy at each maximum density site was calculated using Bader charge analysis code, which was principally developed for electron density analysis [65]. Herein, the isosurface density of Na^+ ion was used instead of charge density. The high-density regions from the MD simulation are slightly different than the reported crystallographic Na sites, which could be because of the simplified form of potential model, where only one type of pair interaction was considered for one type of atomic pair. For instance, even though there are several bond distances for Li-O, we choose only a single Li-O pair of interaction. Depending on the site symmetry, we mark the high-density sites as S1, S2, and S3 [Fig. 6(d)]. Among the three high-density sites, the S1 and S3 find good agreement with the reported crystallographic sites, whereas the site S2 seems an average of a few reported crystallographic Na sites. The occupancy at S1 and S2 is close to unity, whereas close to half occupancy is identified at S3. For cationic channel connectivity, two types of ring connectivity are observed, as marked by circles: ring 1 (sky blue circle) consists of three high-density maxima, whereas ring 2 (orange circle) is formed by two maxima. Furthermore, the sites S2 and S3 are located inside the circles formed by the framework octahedral centers, whereas site S1 is identified on the side of a triangle. None of the Na sites are found on top of the octahedral center because of strong repulsion between the top and bottom octahedra and the Na^+ ions. We also computed the total energies for several site configurations from the first-principles-based structural optimization by choosing several combinations of Na^+ ions among the reported crystallographic Na sites. However, we did not consider all possible combinations, as some of the cases of the Na sites are located at a closer distance ($< 2 \text{ \AA}$). The total energy of the systems was calculated as listed for several configurations in Table III. The combination of Na2 and Na5 shows the lowest energy in favor of crystallographic reported occupancy 0.96 and 0.90, respectively.

The high-density population maxima are indicated on top of the potential energy profile in Fig. 6(e), which reveals a different behavior than the population profile; the potential

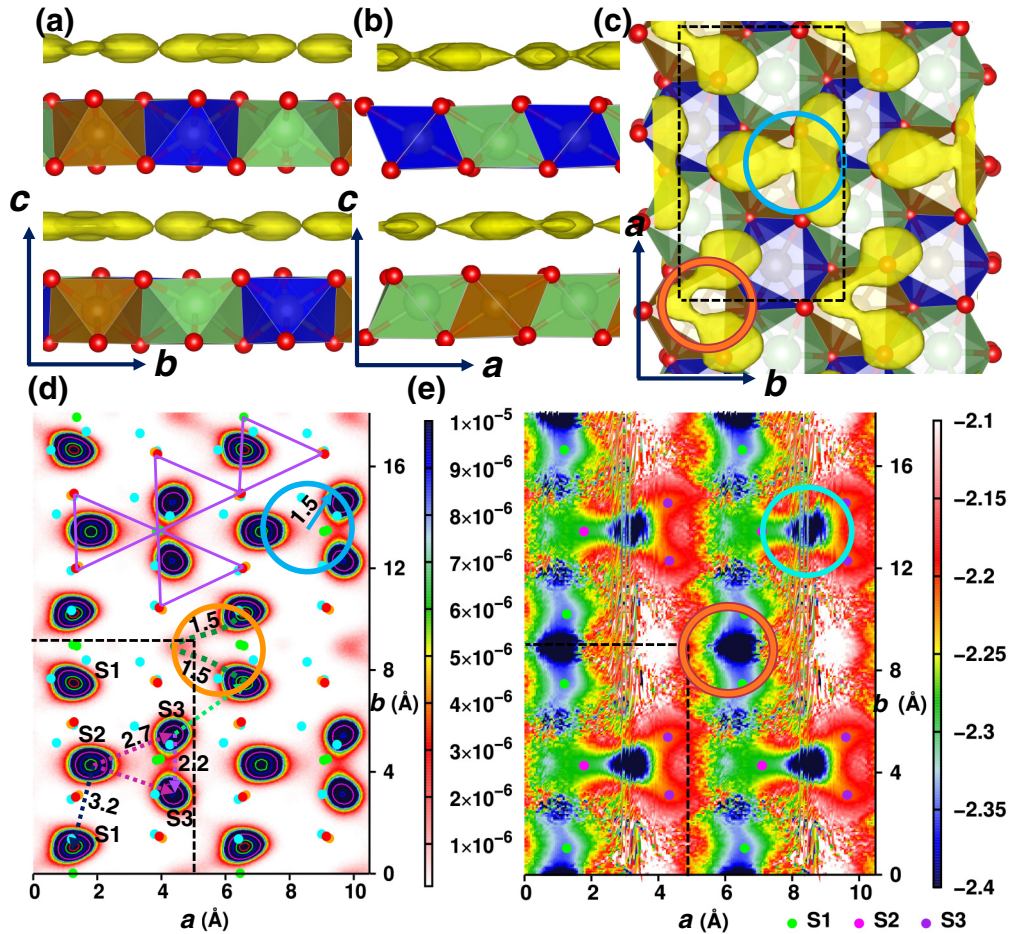


FIG. 6. (a), (b) Side view, and (c) top view of the Na⁺ ion density isosurface (in yellow) with isovalues $5 \times 10^{-6} \text{ \AA}^{-3}$. The octahedral framework structure is also shown. (d) Average population density profiles of the Na⁺ ion for Na₂LiFeTeO₆ in the *ab* plane derived from NVE-MD simulations at 600 K (mapped onto 2×2 unit cells). The locations of the crystallographically distinct Na sites, namely, Na1, Na2, Na3, Na4, Na5, and Na6, are shown in cyan. Three high-density sites identified in MD are marked by S1, S2, and S3. The locations of the crystallographic octahedral centers of Li (orange), Fe (green), and Te (red) are also marked by filled circles. The population density profile indicates two preferred migration paths of the Na⁺ ions: (1) intraring, consisting of two (ring in orange) or three (ring in sky blue) high-density areas and (2) inter-ring, moving from the orange ring to the sky blue ring. The high-density sites S2 and S3 are located inside the purple triangles formed by connecting the octahedral centers, whereas the S1 site is located on an edge of a triangle. (e) Corresponding average potential energy (eV) profile of Na⁺ ions in the *ab* plane. The Na⁺ ion avoids occupying potentially favorable sites by reflecting a low population at potential minima. The locations of the high-density populated sites (S1, S2, and S3) are also marked by circles, as shown in the legends. The unit cell is marked by dotted lines.

energy minima do not match with the population maxima. Essentially, the potential landscape at the conduction plane, provided by the framework octahedra, are modified slightly in presence of more number of Na⁺ ions, particularly, the potential minima are lifted up, as observed in Figs. S3(b) and S4(b) in the Supplemental Material [58]. However, the number of potential energy minima remain the same. For instance, two potential energy minima per layer per unit cell are identified, whereas four Na⁺ ions are available. Thus, the sodium ions cannot occupy the energetically favorable sharp potential energy regions (-2.4 eV), which are lower in number compared to the available Na⁺ ions, but rather occupy the sites which are greater in number and therefore higher in entropy. The difference between the effects of energy and entropy can be linked through Eq. (8), in which entropy plays a significant role. Specifically, particles usually avoid

energetically favorable stiffer potential energy minima with low entropy, whereas they prefer a relatively higher-energy basin which has high entropy. It is worth mentioning that a reaction coordinate ζ as spatial coordinates on the *ab* plane is linked with Boltzmann probability

$$p = \frac{e^{-\Delta F(\zeta)/k_B T}}{Z}, \quad (10)$$

where Z is the partition function. The above expression is valid in a canonical ensemble. Herein, the subsystem consisting of Na⁺ ions is attached with a system consisting of octahedral slabs [46]. Thus, the Na⁺ ions behave like a canonical ensemble at T .

This scenario can be understood by implementing a simulation which places fewer Na⁺ ions in a conducting layer (detailed in Sec. II). The Na⁺ ion density pattern and the po-

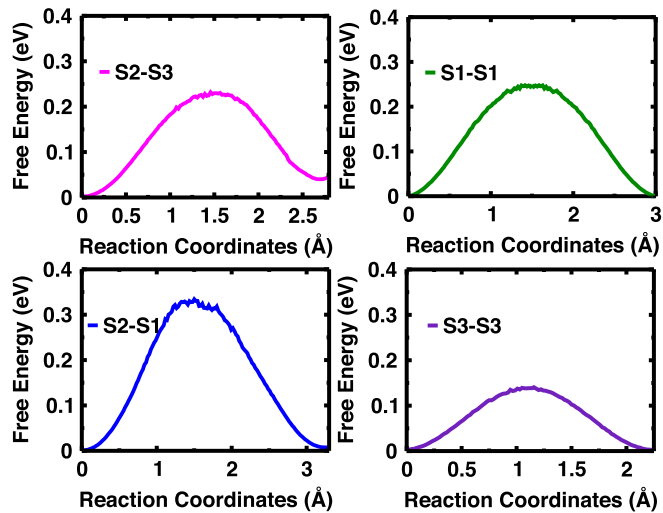


FIG. 7. Free-energy distributions along the straight line connecting pairs of sites of maximum population (S1, S2, and S3). The free-energy distribution is calculated using Eq. (8). Two different (intraring and inter-ring) free-energy distributions are displayed.

tential energy profile are shown in Fig. S3 in the Supplemental Material [58] for the underloaded conduction plane. In the potential energy profile, the locations of the potential energy minima are almost unchanged, whereas the population density pattern changes significantly. Only one type of ring exists, consisting of four high-density maxima. The highest population densities are identified exactly at the potential minima. In this case, the smaller number of Na^+ ions contributes to a lower entropy, resulting in an energy-driven population distribution. The entropy contribution is almost zero if the number of Na^+ ions in the conduction layer is reduced even further, as shown in Fig. S4 (in the Supplemental Material [58]), where all population density maxima and potential minima coincide exactly in the conduction plane, implying a minimal entropic contribution. Such entropic effect is commonly observed in this series, as discussed in $\text{Na}_2\text{Ni}_2\text{TeO}_6$ [30,41].

For a quantitative estimation of the intraring and inter-ring free-energy barrier heights that determine the Na^+ ion diffusion mechanism, the one-dimensional free-energy distributions among the high-density population maxima are shown in Fig. 7. The free energies were calculated by counting the population density distributions inside a rectangle connecting two high-density areas (with a width of 1.0 Å) as indicated in Fig. 6 and projected along a straight line connecting two sites using Eq. (9). Figure 7 captures the free-energy minima and maxima for inter-ring and intraring cases, distinctly, as reflected in Fig. 6. The pairs of site distances and corresponding free-energy barriers of Na^+ ion hopping are listed in Table IV. The inter-ring free-energy barriers are higher than the intraring free-energy barriers, which is also reflected in Fig. 6. Geometrical bottleneck is also one of the major factors for determining the cationic diffusion mechanism, as identified in previous studies [31,60] for $\text{Na}_2\text{Ni}_2\text{TeO}_6$. Looking at the population density pattern for $\text{Na}_2\text{LiFeTeO}_6$, possibly the bottleneck exists between the rings and it influences longer time trapping of cation inside each ring. However, both mechanisms are responsible for the long-range Na^+ ion diffusion.

TABLE IV. Free-energy barrier of Na^+ ions hopping between two population density maxima, as marked on Fig. 6(c), calculated with Eq. (9) at 600 K.

	Between the sites	Site distance (Å)	Barrier height (eV)
Ring 1	S2-S3	2.7	0.23
	S3-S3	2.2	0.14
Ring 2	S1-S1	3.0	0.25
Inter-ring	S2-S1	3.2	0.34

A direct ring mechanism is also revealed by randomly tracking a Na^+ ion over simulation time, as displayed in Fig. 8, where the high-density Na sites (S1, S2, and S3) are also marked. The Na^+ ions diffuse through both the inter-ring and intraring pathways, as evident in the free-energy barriers and the population density profiles.

Both the population density profile and the free-energy profile indicate that the Na^+ ion is trapped for a while within the ring. Therefore, the estimation of the trapping time of the Na^+ ions provides a valuable insight into Na^+ ion diffusion. Thus, the self and van Hove correlation function is calculated [Fig. 9(a)]. The first peak in this figure indicates the thermal oscillation of Na^+ ions in their respective lattice sites, whereas the other peaks signify the Na^+ ions hopping to the neighboring sites. The residence time (the time taken before the second peak arises) of Na^+ ions at the lattice sites is observed to be roughly 10 ~ 15 ps. However, the third peak appears after a significantly longer time (~100 ps) because the Na^+ ions become trapped inside the ring. Furthermore, the trapping time of Na^+ ions inside the ring is also found in a log-log plot of the Na^+ ions' MSD, as shown in Fig. 9(b), which shows a caging of about 100 ps (roughly until the point at which the log-log MSD follows straight-line behavior) with an MSD value of about 4 \AA^2 before moving to the diffusive region. Interestingly, this 4 \AA^2 is close to a value of $d^2/2$, where d is the approximate diameter of a ring (~3 Å). Therefore, the log-log MSD plot also supports the ring mechanism of the dif-

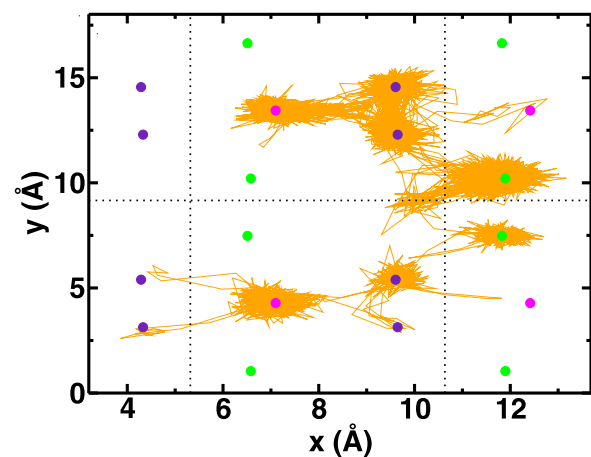


FIG. 8. Trajectory of a randomly chosen Na^+ ion (orange) on the ab plane at 600 K. The maximum density MD sites, S1 (green), S2 (magenta), and S3 (purple), are also marked. The unit cells are indicated by black dotted lines.

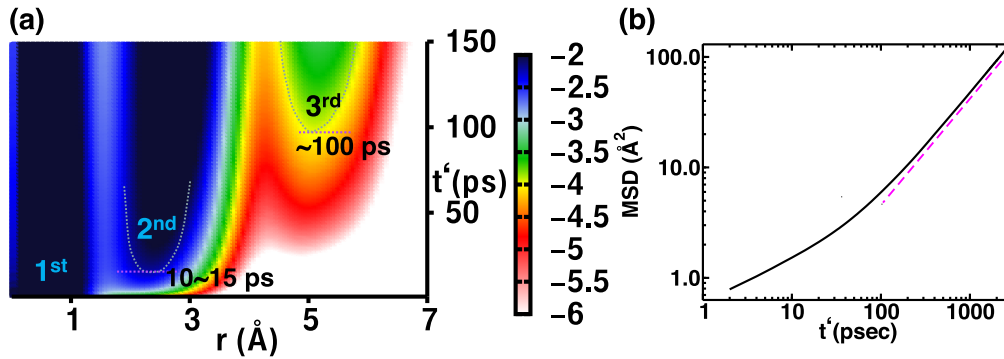


FIG. 9. (a) The self and van Hove correlation $G_s(r, t')$ as a function of radial distance (r) and time (t') for $\text{Na}_2\text{LiFeTeO}_6$ at 600 K from NVE-MD simulations, shown on a logarithmic scale for better visualization. Several high-intensity regions (marked as first, second, and third) indicate the Na^+ ion residential time, while they hop from one site to another neighboring sites. Timescales of just before grow the second and third peaks are also mentioned. (b) A log-log plot of MSD for identifying the ion trapping in a ring. A dotted red line is added to distinguish the caging and diffusive regions.

fusion of the Na^+ ions. The above behavior is also confirmed in the underloaded Na plane for case 1, as displayed in Fig. S3 in the Supplemental Material [58]. In this case, the Na^+ ion also shows trapping inside a ring consisting of four high-density maxima, as revealed in Fig. S3(a) in the Supplemental Material [58]. The corresponding self and van Hove correlation function also reflects a trapping time of about ~ 60 ps in Fig. S5(a) [58]. The same time duration is also identified in the log-log MSD plot in Fig. S5(b) [58].

For further clarity of the Na^+ ion hopping mechanism, the coordination number of the Na^+ ion is analyzed. The first peak at 3 Å of radial distribution function of Na-Na in Fig. 10(a) indicates that if one S3 site is occupied, the nearest S3 site has to remain vacant (the nearest S3-S3 distance is 2.25 Å). The above scenario can be explained using a schematic diagram, as shown in Fig. 10(b). The most likely distribution of Na^+ ions invokes the occupation of two sites of a ring, leaving one site vacant to avoid strong Na-Na

repulsion, as there are six Na sites and four Na^+ ions per layer per unit cell. If there is no Na-site vacancy, no Na^+ ion can move in general. Whereas, in the case of larger Na-site vacancy, the migration mechanism changes significantly, as observed for case 1 [Fig. S3(a) in the Supplemental Material [58]]. Therefore, the Na-site vacancy is one of the responsible factors for such ring mechanism, and the Na^+ ions can show a circular motion inside the rings, or they can move out from the ring. When one Na^+ ion moves out from a ring, another Na^+ ion should enter from a neighboring ring to maintain local charge balance. If these ions show a circular motion within a ring, the duration should be close to 100 ps, as identified in the log-log plot of the MSD in Fig. 9(b).

IV. CONCLUSION

A refined set of interatomic models represents the structural and transport properties of honeycomb-layered oxides in

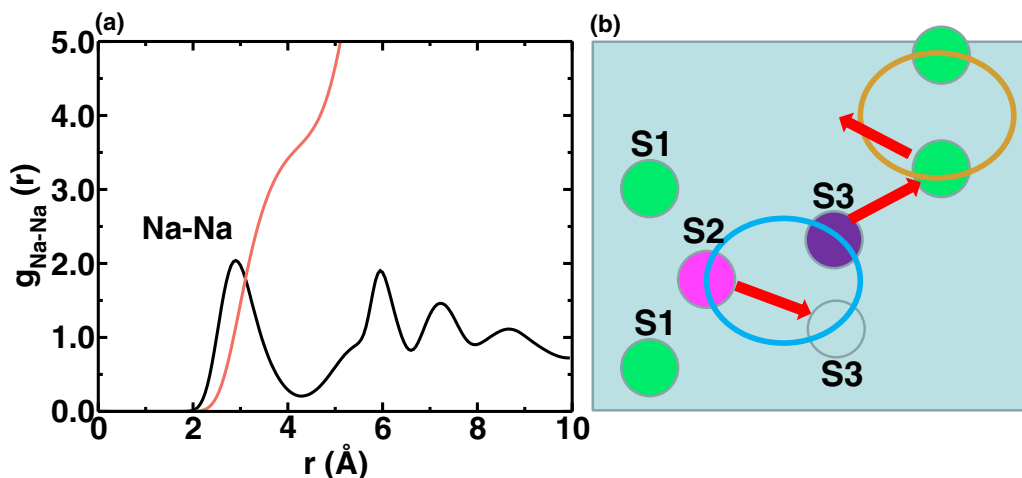


FIG. 10. (a) The Na-Na radial distribution function (black), $g_{\text{Na-Na}}(r)$, and its integration in a coordination number plot (red). (b) A schematic representation of the Na^+ ion hopping mechanism within the Na sublattice. The filled circle represents the occupied Na sites (different colors indicates different Na sites); the open circle indicates the vacant Na sites; the arrow indicates the direction of Na^+ ion hopping.

$\text{Na}_2\text{LiFeTeO}_6$, in excellent agreement with the experimental results. This potential model can be leveraged to garner distinct atomistic insights such as the entropic contribution in cationic distribution and the ringlike cationic diffusion from the population density profile, the free-energy barrier, the self and van Hove correlation, and the log-log MSD plot. Therefore, the MD simulation provides an avenue to test the ion dynamics of various honeycomb-layered oxides. Particularly, the entropic contribution in cationic distribution and the distinct ringlike feature that controls fast ion transport in solids is interesting in applications beyond honeycomb-layered oxides.

ACKNOWLEDGMENTS

K.S. thanks the JSPS International Fellowship (Grant No. 21F21345) and acknowledges Professor P. Kumar Padmanabhan for his fruitful suggestions. This work was partially supported by the TEPCO Memorial Foundation. We gratefully acknowledge the Center for Computational Materials Science of Institute for Materials Research, Tohoku University, for permitting the use of MASAMUNE-IMR (MAterial science Supercomputing system for Advanced MULtiscala simulations toward NExt-generation Institute of Material Research) (Project No. 20S0021).

-
- [1] C. R. A. Catlow, Z. X. Guo, M. Miskufova, S. A. Shevlin, A. G. H. Smith, A. A. Sokol, A. Walsh, D. J. Wilson, and S. M. Woodley, *Advances in computational studies of energy materials*, *Philos. Trans. R. Soc. A* **368**, 3379 (2010).
- [2] J. Kawamura, R. Asayama, N. Kuwata, and O. Kamishima, Ionic transport in glass and polymer: Hierarchical structure and dynamics, in *Physics of Solid State Ionics*, edited by T. Sakuma and H. Takahashi, Vol. 81 (Research Sighpost, Kerala, India, 2006), pp. 193–246.
- [3] A. R. Kulkarni, H. S. Maiti, and A. Paul, Fast ion conducting lithium glasses, *Bull. Mater. Sci.* **6**, 201 (1984).
- [4] A. Hayashi, K. Noi, A. Sakuda, and M. Tatsumisago, Superionic glass-ceramic electrolytes for room-temperature rechargeable sodium batteries, *Nat. Commun.* **3**, 856 (2012).
- [5] P. Bron, S. Johansson, K. Zick, J. Schmedt auf der Gunne, S. Dehnen, and B. Roling, $\text{Li}_{10}\text{SnP}_2\text{S}_{12}$: An affordable lithium superionic conductor, *J. Am. Chem. Soc.* **135**, 15694 (2013).
- [6] C. Masquelier, Lithium ions on the fast track, *Nat. Mater.* **10**, 649 (2011).
- [7] N. Kamaya, K. Homma, Y. YamaNawa, M. Hirayama, R. Kanno, and M. Yonemura, T. Kamiyama, Y. Kato, S. Hama, K. Kawamoto, and A. Mitsui, A lithium superionic conductor, *Nat. Mater.* **10**, 682 (2011).
- [8] S. Adams and R. P. Rao, Structural requirements for fast lithium ion migration in $\text{Li}_{10}\text{GeP}_2\text{S}_{12}$, *J. Mater. Chem.* **22**, 7687 (2012).
- [9] K. Takada, Progress and prospective of solid-state lithium batteries, *Acta Mater.* **61**, 759 (2013).
- [10] G. Sahu, Z. Lin, J. Li, Z. Liu, N. Dudney, and C. Liang, Air-stable, high-conduction solid electrolytes of arsenic-substituted Li_4SnS_4 , *Energy Environ. Sci.* **7**, 1053 (2014).
- [11] M. Park, X. Zhang, M. Chung, G. B. Less, and A. M. Sastry, A review of conduction phenomena in li-ion batteries, *J. Power Sources* **195**, 7904 (2010).
- [12] M. Sathiya, K. Ramesha, G. Rouse, D. Foix, D. Gonbeau, K. Guruprakash, A. S. Prakash, M.-L. Doublet, and J.-M. Tarascon, Li_4NiTe_6 as a positive electrode for li-ion batteries, *Chem. Commun.* **49**, 11376 (2013).
- [13] K. Saranya, C. Deviannapoorani, L. Dhivya, S. Ramakumar, N. Janani, and R. Murugan, $\text{Li}_{7-x}\text{La}_3\text{Sn}_{2-x}\text{Nb}_x\text{O}_{12}$ ($x = 0.251$) ($x = 0.25-1$) cubic lithium garnet, *Mater. Lett.* **77**, 57 (2012).
- [14] V. Thangadurai, S. Narayanan, and D. Pinzaru, Garnet-type solid-state fast Li ion conductors for Li batteries: Critical review, *Chem. Soc. Rev.* **43**, 4714 (2014).
- [15] G. M. Kanyolo, T. Masese, N. Matsubara, C.-Y. Chen, J. Rizell, Z.-D. Huang, Y. Sassa, M. Månsson, H. Senoh, and H. Matsumoto, Honeycomb layered oxides: structure, energy storage, transport, topology and relevant insights, *Chem. Soc. Rev.* **50**, 3990 (2021).
- [16] A. J. Brown, Q. Xia, M. Avdeev, B. J. Kennedy, and C. D. Ling, Synthesis-controlled polymorphism and magnetic and electrochemical properties of $\text{Li}_3\text{Co}_2\text{SbO}_6$, *Inorg. Chem.* **58**, 13881 (2019).
- [17] N. S. Grundish, I. D. Seymour, G. Henkelman, and J. B. Goodenough, Electrochemical properties of three $\text{Li}_2\text{Ni}_2\text{Te}_6$ structural polymorphs, *Chem. Mater.* **31**, 9379 (2019).
- [18] Z. Yang, Y. Jiang, L. Deng, T. Wang, S. Chen, and Y. Huang, A high-voltage honeycomb-layered $\text{Na}_4\text{NiTeO}_6$ as cathode material for na-ion batteries, *J. Power Sources* **360**, 319 (2017).
- [19] D. Yuan, X. Liang, L. Wu, Y. Cao, X. Ai, J. Feng, and H. Yang, A honeycomb-layered $\text{Ni}_3\text{Ni}_2\text{SbO}_6$: A high-rate and cycle-stable cathode for sodium-ion batteries, *Adv. Mater.* **26**, 6301 (2014).
- [20] T. Masese, K. Yoshii, Y. Yamaguchi, T. Okumura, Z.-D. Huang, M. Kato, K. Kubota, J. Furutani, Y. Orikasa, H. Senoh *et al.*, Rechargeable potassium-ion batteries with honeycomb-layered tellurates as high voltage cathodes and fast potassium-ion conductors, *Nat. Commun.* **9**, 3823 (2018).
- [21] T. Masese, K. Yoshii, M. Kato, K. Kubota, Z.-D. Huang, H. Senoh, and M. Shikano, A high voltage honeycomb layered cathode framework for rechargeable potassium-ion battery: P2-type $\text{K}_{2/3}\text{Ni}_{1/3}\text{Co}_{1/3}\text{Te}_{1/3}\text{O}_2$, *Chem. Commun.* **55**, 985 (2019).
- [22] K. Yoshii, T. Masese, M. Kato, K. Kubota, H. Senoh, and M. Shikano, Sulfonylamide-based ionic liquids for high-voltage potassium-ion batteries with honeycomb layered cathode oxides, *Chem. Electro. Chem.* **6**, 3901 (2019).
- [23] C.-Y. Chen, J. Rizell, G. M. Kanyolo, T. Masese, Y. Sassa, M. Månsson, K. Kubota, K. Matsumoto, R. Hagiwara, and Q. Xu, High-voltage honeycomb layered oxide positive electrodes for rechargeable sodium batteries, *Chem. Commun.* **56**, 9272 (2020).
- [24] D. S. Bhande, G. Ali, D.-H. Kim, D. A. Anang, T. J. Shin, M.-G. Kim, Y.-M. Kang, K. Y. Chung, and K.-W. Nam, Honeycomb-layer structured $\text{Na}_3\text{Ni}_2\text{BiO}_6$ as a high voltage and long life cathode material for sodium-ion batteries, *J. Mater. Chem. A* **5**, 1300 (2017).
- [25] J. Ma, S.-H. Bo, L. Wu, Y. Zhu, C. P. Grey, and P. G. Khalifah, Ordered and disordered polymorphs of $\text{Na}(\text{Ni}_{2/3}\text{Sb}_{1/3})\text{O}_2$:

- Honeycomb-ordered cathodes for Na-Ion batteries, *Chem. Mater.* **27**, 2387 (2015).
- [26] A. Gupta, C. Buddie Mullins, and J. B. Goodenough, Na₂Ni₂TeO₆: evaluation as a cathode for sodium battery, *J. Power Sources* **243**, 817 (2013).
- [27] L. Zheng and M. N. Obrovac, Honeycomb compound Na₃Ni₂BiO₆ as positive electrode material in Na cells, *J. Electrochem. Soc.* **163**, A2362 (2016).
- [28] M. Aniya, Understanding the mechanism of superionic transport from trends of materials properties, *Phys. Procedia* **44**, 25 (2013).
- [29] M. Saiful Islam and C. A. J. Fisher, Lithium and sodium battery cathode materials: Computational insights into voltage, diffusion and nanostructural properties, *Chem. Soc. Rev.* **43**, 185 (2014).
- [30] K. Sau and P. Padma Kumar, Ion transport in na2m2teo6: insights from molecular dynamics simulation, *J. Phys. Chem. C* **119**, 1651 (2015).
- [31] K. Sau, T. Ikeshoji, G. M. Kanyolo, and T. Masese, Modelling cationic diffusion in nickel-based honeycomb layered tellurates using vashishta-rahman interatomic potential and relevant insights, *ChemRxiv* (Cambridge Open Engage, Cambridge, 2021), doi:10.26434/chemrxiv.13522076.v4.
- [32] S. K. Karna, Y. Zhao, R. Sankar, M. Avdeev, P. C. Tseng, C. W. Wang, G. J. Shu, K. Matan, G. Y. Guo, and F. C. Chou, Sodium layer chiral distribution and spin structure of Na₂Ni₂TeO₆ with a ni honeycomb lattice, *Phys. Rev. B* **95**, 104408 (2017).
- [33] A. Kumar Bera and S. M. Yusuf, Temperature-dependent n-ion conduction and its pathways in the crystal structure of the layered battery material Na₂Ni₂TeO₆, *J. Phys. Chem. C* **124**, 4421 (2020).
- [34] V.B. Nalbandyan, D. D. Petrenko, and M.A. Evstigneeva, Heterovalent substitutions in Na₂M₂TeO₆ family: Crystal structure, fast sodium ion conduction and phase transition of Na₂LiFeTeO₆, *Solid State Ionics* **233**, 7 (2013).
- [35] B. Hafskjold and X. Li, Molecular dynamics simulations of the Mg²⁺-stabilized Na⁺-beta"-alumina, *J. Phys.: Condens. Matter* **7**, 2949 (1995).
- [36] M. A. Zendejas and J. O. Thomas, Conduction mechanisms in solid electrolytes: Na+ beta-alumina, *Phys. Scr.* **T33**, 235 (1990).
- [37] S. Edvardsson, L. Ojamae, and J. O. Thomas, A study of vibrational modes in Na⁺ beta-alumina by molecular dynamics simulation, *J. Phys.: Condens. Matter* **6**, 1319 (1994).
- [38] Z. Skotniczny, J. Moscinski, and Z. Rycerz, Computer simulation studies of cation migration mechanisms in sodium beta-alumina, *J. Phys. C: Solid State Phys.* **19**, 4781 (1986).
- [39] O. Pankratov, H. Huang, T. Diaz de la Rubia, and C. Mailhot, As-vacancy interaction and ring mechanism of diffusion in si, *Phys. Rev. B* **56**, 13172 (1997).
- [40] J. Zhang, Y. Ashizawa, and H. Oka, First principles study of as-vacancy interaction and the ring mechanism of diffusion in the presence of Ge in Si, *J. Phys.: Condens. Matter* **18**, 4879 (2006).
- [41] K. Sau and P Padma Kumar, Role of ion-ion correlations on fast ion transport: Molecular dynamics simulation of Na₂Ni₂TeO₆, *J. Phys. Chem. C* **119**, 18030 (2015).
- [42] P. Vashishta and A. Rahman, Ionic motion in α -AgI, *Phys. Rev. Lett.* **40**, 1337 (1978).
- [43] R. A. Buckingham, The classical equation of state of gaseous helium, neon and argon, *Proc. R. Soc. London, Ser. A* **168**, 264 (1938).
- [44] J. E. Lennard-Jones, Cohesion, *Proc. Phys. Soc.* **43**, 461 (1931).
- [45] K. Sau, T. Ikeshoji, and S. Roy, Role of divalent cation (ba) substitution in the Li⁺ ion conductor LiTi₂(PO₄)₃: A molecular dynamics study, *Phys. Chem. Chem. Phys.* **22**, 14471 (2020).
- [46] P. Padma Kumar and S. Yashonath, Structure, conductivity, and ionic motion in Na_{1+x}Zr₂Si_xP_{3-x}O₁₂: A simulation study, *J. Phys. Chem. B* **106**, 7081 (2002).
- [47] K. Pramanik, K. Sau, and P. Padma Kumar, Role of framework flexibility in ion transport: A molecular dynamics study of LiM₂^{IV}(PO₄)₃, *J. Phys. Chem. C* **124**, 4001 (2020).
- [48] M. Parrinello and A. Rahman, Polymorphic transitions in single crystals: A new molecular dynamics method, *J. Appl. Phys.* **52**, 7182 (1981).
- [49] S. Plimpton, Fast parallel algorithms for short-range molecular dynamics, *J. Comput. Phys.* **117**, 1 (1995).
- [50] A. R. Miedema, The electronegativity parameter for transition metals: Heat of formation and charge transfer in alloys, *J. Less-Common Met.* **32**, 117 (1973).
- [51] G. Kresse and J. Hafner, *Ab initio* molecular dynamics for liquid metals, *Phys. Rev. B* **47**, 558 (1993).
- [52] P. E. Blöchl, Projector augmented-wave method, *Phys. Rev. B* **50**, 17953 (1994).
- [53] G. Kresse and D. Joubert, From ultrasoft pseudopotentials to the projector augmented-wave method, *Phys. Rev. B* **59**, 1758 (1999).
- [54] Y. Wang, W. D. Richards, S. P. Ong, L. J. Miara, J. C. Kim, Y. Mo, and G. Ceder, Design principles for solid-state lithium superionic conductors, *Nat. Mater.* **14**, 1026 (2015).
- [55] K. Sau and T. Ikeshoji, Origin of Fast Ion Conduction in Na₃PS₄: Insight from Molecular Dynamics Study, *J. Phys. Chem. C* **124**, 20671 (2020).
- [56] K. Sau, T. Ikeshoji, S. Kim, S. Takagi, and S. Ichi Orimo, Comparative Molecular Dynamics Study of the Roles of Anion-Cation and Cation-Cation Correlation in Cation Diffusion in Li₂B₁₂H₁₂ and LiCB₁₁H₁₂, *Chem. Mater.* **33**, 2357 (2021).
- [57] P. Hopkins, A. Fortini, A. J. Archer, and M. Schmidt, The van hove distribution function for brownian hard spheres: Dynamical test particle theory and computer simulations for bulk dynamics, *J. Chem. Phys.* **133**, 224505 (2010).
- [58] See Supplemental Material at <http://link.aps.org/supplemental/10.1103/PhysRevMaterials.6.045406> for coordination number analysis, population density distribution, potential energy distribution on the conduction plane, and self van Hove correlation function and logarithmic MSD.
- [59] N. Nitta, F. Wu, J. T. Lee, and G. Yushin, Li-ion battery materials: Present and future, *Mater. Today* **18**, 252 (2015).
- [60] M. A. Evstigneeva, V. B. Nalbandyan, A. A. Petrenko, B. S. Medvedev, and A. A. Kataev, A new family of fast sodium ion conductors: Na₂M₂TeO₆ (M = Ni, Co, Zn, Mg), *Chem. Mater.* **23**, 1174 (2011).
- [61] M. Tuckerman, *Statistical Mechanics: Theory and Molecular Simulation* (Oxford University Press, Oxford, 2010)

- [62] B. L. Bhargava and S. Balasubramanian, Dynamics in a room-temperature ionic liquid: A computer simulation study of 1, 3-dimethylimidazolium chloride, *J. Chem. Phys.* **123**, 144505 (2005).
- [63] J. P. Hansen and I. R. McDonald, Statistical mechanics of dense ionized matter. IV. density and charge fluctuations in a simple molten salt, *Phys. Rev. A* **11**, 2111 (1975).
- [64] F. Dommert, J. Schmidt, B. Qiao, Y. Zhao, C. Krekeler, L. Delle Site, R. Berger, and C. Holm, A comparative study of two classical force fields on statics and dynamics of [EMIM] [BF₄] investigated via molecular dynamics simulations, *J. Chem. Phys.* **129**, 224501 (2008).
- [65] G. Henkelman, A. Arnaldsson, and H. Jónsson, A fast and robust algorithm for bader decomposition of charge density, *Comput. Mater. Sci.* **36**, 354 (2006).